

# Synthesis of Layered Double Hydroxides and TiO<sub>2</sub> Supported Metal Nanoparticles for Electrocatalysis

Adefunke O. Koyejo,<sup>[a, b]</sup> Lokesh Kesavan,<sup>[b]</sup> Pia Damlin,<sup>[b]</sup> Mikko Salomäki,<sup>[b]</sup> and Carita Kvarnström\*<sup>[b]</sup>

In the present work, solution-phase synthesis was employed to prepare two sets of catalysts with different transition metals as active sites. One set contained Au or Pd supported on TiO<sub>2</sub> (Au–TiO<sub>2</sub>, Pd–TiO<sub>2</sub>), whereas the other set contained layered double hydroxides (NiFe-LDH and CuFe-LDH). The electrocatalytic performance of these composite materials was investigated by cyclic voltammetry (CV) using a model compound 4-nitrophenol (4-NP). Composite materials were characterized by various analytical techniques to gain insight into the catalysts active sites. The morphology and structure of the prepared samples were investigated by X-ray diffraction, attenuated total reflectance Fourier transform infrared, X-ray photoelectron spectroscopy, transmission scanning electron microscope, and

field emission scanning electron microscope. Metal nanoparticles loading on TiO<sub>2</sub> was measured by inductively coupled plasma – optical emission spectrometry. CV measurements were performed in acetonitrile solution containing 0.1 M tetrabutylammonium hexafluorophosphate (TBAPF<sub>6</sub>) and 1 mM 4-NP. Among all dioxides (Au–TiO<sub>2</sub>, Pd–TiO<sub>2</sub>) and hydroxides (NiFe-LDH and CuFe-LDH) studied, Pd–TiO<sub>2</sub> shows the lowest onset potential (–0.32 V vs. Ag/AgCl) for the electrocatalytic reduction of 4-NP. This is the first comparative study of such materials for 4-NP electrocatalysis in aprotic solvent, thus demonstrating the suitability of dioxide and hydroxide based materials as electrocatalysts.

## Introduction

Solution phase synthesis of nanomaterials/composites has emerged as a leading technique in improving catalytic performance of composite materials.<sup>[1]</sup> Metal nanoparticles are especially of great importance due to their tunable physicochemical properties and extensive application range in the field of surface science, drug delivery, biomedical diagnosis and energy storage.<sup>[2]</sup> However, their use is somewhat limited by availability, cost and the tendency of nanoscale particles to agglomerate. These disadvantages can be resolved by the use of supporting materials.<sup>[3]</sup> Among the supporting materials, semiconductor oxides (especially TiO<sub>2</sub>) are widely used. TiO<sub>2</sub> has been extensively used as a support material because of its low cost, stability,<sup>[4]</sup> strong interaction effect with metals, good physio-chemical properties and high stability in acid and alkaline solutions.<sup>[5]</sup> On the other hand, layered double hydrox-

ides (LDHs) have also attracted attention because of ease of synthesis, unique structure and uniform distribution of several metal cations in the brucite layer.<sup>[6]</sup> Chemically, LDHs are multilayer di/trivalent metal double hydroxides with cationic brucite layer and intercalating anionic layers enriched with water and hydroxyl ions. LDHs often exhibit a huge surface area and pore volume, which enables them to be used in surface catalysis.<sup>[7]</sup> Currently, LDHs are widely explored in several applications such as anion exchange,<sup>[8]</sup> electrochemical sensors<sup>[9]</sup> and as catalysts in water treatment.<sup>[10]</sup> The constant increase in the number of toxic organic compounds in the environment, mainly from pharmaceutical and pigments industry has raised a lot of attention over the years. The synthesis of suitable catalysts for the reduction and conversion of these organic compounds to valuable products or chemicals is critical both in academics and in industrial processes.<sup>[11]</sup> Among these toxic compounds, nitrophenols are one of the persistent, with 4-nitrophenol (4-NP) being the most hazardous in the phenol group.<sup>[12]</sup> Due to its toxicity, 4-NP has been studied as a model compound to evaluate the catalytic activity of nanoparticles and other solid state materials<sup>[13]</sup> by adopting several methods such as mass spectrometry, chromatography and spectrophotometry.<sup>[14]</sup> However, the complexity of sample preparation and laborious nature makes these methods cumbersome. The electrochemical reduction methods, based on chemically modified electrodes have been of great interest because of their ease of operation, reproducibility, high conductivity, selectivity and increased surface area.<sup>[15]</sup> The electrocatalytic performance of 4-NP reduction is dependent on the electrode material, electrolyte medium, and the solvent.<sup>[16]</sup> Some of the materials reported and tested for the detection and reduction of 4-NP include: Gold,<sup>[17]</sup> boron,<sup>[18]</sup> zeolite,


[a] A. O. Koyejo

University of Turku Graduate School (UTUGS)  
Doctoral Programme in Exact Sciences (EXACTUS)  
Henrikinkatu 2, 20500 Turku, Finland

[b] A. O. Koyejo, Dr. L. Kesavan, Dr. P. Damlin, Dr. M. Salomäki,

Prof. C. Kvarnström  
Department of Chemistry, Turku University Centre for Materials and Surfaces (MatSurf)  
University of Turku  
Henrikinkatu 2, 20500 Turku, Finland  
E-mail: carkva@utu.fi

 Supporting information for this article is available on the WWW under <https://doi.org/10.1002/celec.202200442>

 © 2022 The Authors. ChemElectroChem published by Wiley-VCH GmbH. This is an open access article under the terms of the Creative Commons Attribution License, which permits use, distribution and reproduction in any medium, provided the original work is properly cited.

mercury, and silver<sup>[19]</sup> either in the form of pure metal electrodes or metal composites electrodes. Satisfactory results have been obtained but until this date, most studies have only focused on detection and reduction of 4-NP in aqueous media, with little or no information available in aprotic solvents. Although water has beneficial properties such as low viscosity, low toxicity low cost, it still has a limited thermodynamic stability window for electrochemical studies.<sup>[20]</sup> This limits the range of detectable redox couples and increases the probability of unwanted electron transfer reactions between the solvent and the electrode. Non-aqueous solvents are therefore, of interest for electrochemical reactions because they improve the solubility of reactants, reactivity of adsorbed species, and the formation of products. In view of these, the goal was to prepare and characterize two set of nanomaterials consisting of dioxides (Au–TiO<sub>2</sub>, Pd–TiO<sub>2</sub>) and double hydroxides (NiFe-LDH and CuFe-LDH), both having a transition metals as their catalytically active component. The first set of materials (Au–TiO<sub>2</sub>, Pd–TiO<sub>2</sub>) offer metal active centres in zero oxidation state and the second set of materials (NiFe-LDH and CuFe-LDH) delivers metal active centres in +2/+3 oxidation state. In the case of TiO<sub>2</sub> (tetragonal),<sup>[21]</sup> Au or Pd nanoparticles (freely exposed metal atoms) decorated on TiO<sub>2</sub>, and Au↔TiO<sub>2</sub>, Pd↔TiO<sub>2</sub> interstitial sites were considered to be catalytically active centres.<sup>[22,23]</sup> Whereas with LDHs, the cationic metal brucite layers (tetrahedral)<sup>[24]</sup> were presumed to be the catalytic active centres. The choice of material was also based on their semiconducting nature, which makes them useful for further photoelectrochemical studies. These materials were evaluated for their suitability in 4-NP electroreduction. Here, we compared the material sets like a) Au–TiO<sub>2</sub> vs. Pd–TiO<sub>2</sub> b) NiFe-LDH vs. CuFe-LDH c) a comparison of materials (a) vs. (b). This will reveal how the performance varies between a) two different metal nanoparticles anchored on a same support b) two different LDHs, along with c) cross-functional comparison (NPs vs. LDHs). Thus, this work also serves the purpose of catalysts screening for 4-NP electro-reduction. Further, the motivation to pick materials like TiO<sub>2</sub> and LDHs was that these materials are widely used in photo-catalysis in many chemical transformations,<sup>[25,26]</sup> e.g. degradation of environmentally impactful pollutant compounds, but their role in electro-catalysis has been studied sparsely until now. TiO<sub>2</sub> & LDHs do possess suitable bandgap to harvest photons and supply energy to reactant molecule (e.g. Orange II dye, 4-NP). The surface of these materials were shown to activate the –N=N–, –O–N=O, –O–C=O bonds and convert them into desirable products (–NH<sub>2</sub>, –C–O–C=O).<sup>[27,28]</sup> However, can we operate these materials for electro-catalysis? Therefore, to widen their scope and explore their applicability; these materials were of primary interest in our investigation.

## Experimental Section

### Chemical reagents

Nickel (II) nitrate hexahydrate (Ni(NO<sub>3</sub>)<sub>2</sub>·6H<sub>2</sub>O, Sigma-Aldrich), Iron (II) nitrate nonhydrate (Fe(NO<sub>3</sub>)<sub>3</sub>·9H<sub>2</sub>O, Sigma-Aldrich), Sodium

tetrachloropalladate (Na<sub>2</sub>PdCl<sub>4</sub>, 98%), copper nitrate trihydrate (Cu(NO<sub>3</sub>)<sub>2</sub>·3H<sub>2</sub>O, Sigma-Aldrich), sulfuric acid (H<sub>2</sub>SO<sub>4</sub>, Sigma-Aldrich), Hydrogen tetrachloroaurate (III) hydrate (HAuCl<sub>4</sub>·H<sub>2</sub>O, Alfa Aesar), titanium dioxide (TiO<sub>2</sub>, Degussa, P25), sodium hydroxide (NaOH, Sigma-Aldrich), sodium carbonate (Na<sub>2</sub>CO<sub>3</sub>, FF chemicals, 99.8%), Polyvinyl alcohol (PVA, Merck) hydrogen chloride (HCl, Fisher Scientific) and acetonitrile (ACN, VWR chemicals, 99.8%) were used without further purification. Tetrabutylammonium hexafluorophosphate (TBAPF<sub>6</sub>, TCI, 99%) and 4-nitrophenol (4-NP, Aldrich) were dried in a vacuum oven at 70 °C for 1 h prior to use.

## Synthesis of catalysts

### Synthesis of TiO<sub>2</sub> supported monometallic catalysts (1% Au–TiO<sub>2</sub> and 1%Pd–TiO<sub>2</sub>)

The synthesis of nanoparticle catalyst follows our earlier reported method.<sup>[29]</sup> The Au supported catalysts were prepared by mixing desired amount of an aqueous solution of HAuCl<sub>4</sub>·H<sub>2</sub>O (1 mM) and PVA in a beaker with constant stirring for 5 min (The PVA to Au ratio was 1:1 wt%). Then freshly prepared NaBH<sub>4</sub> (0.1 M) aqueous solution was added to the above mixture and stirred for another 30 min. This led to a colour change from yellow to wine red. Thereafter, 495 mg of the support material (TiO<sub>2</sub>) was added to the Au colloid. The pH was adjusted to 4–5 using conc. H<sub>2</sub>SO<sub>4</sub> and allowed to stir for 1 h for the complete immobilization of Au on TiO<sub>2</sub>. The mixture was then filtered and washed with 500 mL of DI water and dried at 110 °C overnight. The sample was collected and labelled 1% Au–TiO<sub>2</sub>. 1% Pd–TiO<sub>2</sub> was synthesized under identical conditions. For Pd, the colour change was from yellow to dark brown.

### Synthesis of LDH samples (NiFe-LDH and CuFe-LDH)

LDH samples<sup>[30]</sup> were synthesized by a co-precipitation method<sup>[30]</sup> in which aqueous solutions of metal salts Ni(NO<sub>3</sub>)<sub>2</sub>·6H<sub>2</sub>O and Fe(NO<sub>3</sub>)<sub>3</sub>·9H<sub>2</sub>O were mixed in a ratio of 3:1 in 500 mL H<sub>2</sub>O. Then a solution of NaOH (2 M) and Na<sub>2</sub>CO<sub>3</sub> (2 M) was simultaneously added to the above mixture at a rate of 1 mL min<sup>-1</sup> to maintain a co-precipitation at the pH of 10.5 ± 0.5. The resultant slurry was stirred for 30 min. Then, the LDH materials were filtered and washed repeatedly until a pH of 7 was attained and all impurities were removed. The obtained sample was aged in a digestion bomb at 110 °C for 4 h for the crystallization of LDH. The particles were thereafter, filtered and dried overnight at 110 °C. LDH samples were then crushed into a fine powder and labelled NiFe-LDH. CuFe LDH was synthesized under identical conditions.

### Electrochemical measurement

All electrochemical experiments were performed using a computer aided Autolab PGSTAT101 potentiostat in a potential range of 0 V–(–2.0 V) at a scan rate of 50 mV/s. A glass cell

comprising of a three-electrode arrangement was used. Catalyst modified glassy carbon electrode (GCE, 2 mm diameter) was used as the working electrode, an Ag/AgCl wire as a pseudo reference and a Pt wire as the counter electrode. Prior to each measurement, the GCE was polished with 6, 3, 1, and  $\frac{1}{4}$   $\mu\text{m}$  diamond paste, then rinsed with DI water and ethanol. The reference electrode was calibrated against ferrocene ( $E_{1/2}(\text{Fe}/\text{Fe}^+) = 0.45 \text{ V}$ ) in TBAPF<sub>6</sub> and acetonitrile.

### Preparation of catalyst modified electrode

A dispersion of 1 mg of as-synthesized catalyst in 1 mL of ethanol was sonicated for 10 min. Further, 30  $\mu\text{L}$  of the dispersion was drop-casted on the GCE (Geometric surface area: 3.14 mm<sup>2</sup>) and dried at room temperature. The modified GCE electrode, Pt wire and Ag/AgCl electrode were inserted into the electrochemical cell filled with 5 mL of the electrolyte solution containing 0.1 M TBAPF<sub>6</sub> in ACN and 4-NP (1 mM). Prior to each experiment, the electrolyte solution was deaerated under nitrogen atmosphere for 10 min.

### Characterization

To identify the crystalline phase present in each catalyst, XRD technique was applied. As-synthesized catalyst was analysed at room temperature using a Huber G670 detector and copper  $K_{\alpha 1}$  radiation ( $\lambda = 1.5406 \text{ \AA}$ ). The  $2\theta$  measurement angle ranged from  $5^\circ$ – $100^\circ$  with an exposure time of 30 min followed by 10 data reading scans of the imaging plate. A Bruker Vertex 70 FTIR spectrometer equipped with a Harrick VideoMVP™ diamond ATR accessory was used to measure the infrared spectrum over the spectral region of 4000 to 450  $\text{cm}^{-1}$ . A total of 32 scans was collected and a resolution of 4  $\text{cm}^{-1}$  was used. The morphology of TiO<sub>2</sub> supported nanoparticles (Au–TiO<sub>2</sub> and Pd–TiO<sub>2</sub>) was investigated by TEM (JEM-1400 Plus) with a resolution of 0.38 nm. For the analyses, 1 mg of catalyst was dispersed in ethanol and sonicated for 10 min. A drop of the dispersion was placed on a TEM grid and allowed to air dry. The prepared sample was used for visually analysis using an OSIS Quemesa 11 camera at an acceleration voltage of 120 kV. Particle size was measured by image J software. The surface characterization of LDH materials was studied using a Thermo-scientific Apreo S FE-SEM. 1 mg of sample was dispersed in ethanol and 3  $\mu\text{L}$  was drop-casted on a silicon wafer and air dried. The samples were analysed at an accelerating voltage of 2.00 kV at different resolutions like 4000X, 12700X and 100000X. A Thermo Scientific Nexsa Surface Analysis System with Al  $K_{\alpha}$  radiation was used to analyse the elemental composition and chemical state of as-synthesized catalysts. Adventitious carbon was used as a calibration reference at 284.8 eV. The catalytically active metal content present in (1%) Au–TiO<sub>2</sub> and (1%) Pd–TiO<sub>2</sub> were determined by inductively coupled plasma-optical emission spectrometry (ICP-OES) using an Agilent 5900 SVDV ICP-OES – RAMI Model. Samples were prepared for ICP-OES analysis by dissolving the catalysts in a

mixture of HNO<sub>3</sub> and HCl. (See Supporting Information for details)

## Results and Discussion

### Characterization of catalyst materials

XRD measurements were performed to confirm the formation and the crystalline nature of as-synthesized catalysts (Figure 1). The supported monometallic Au and Pd catalysts (Au–TiO<sub>2</sub> and Pd–TiO<sub>2</sub>) shows the  $2\theta$  values at 25.2, 36.9, 37.3, 38.5, 48.0, 53.8, 55.0, 62.6 which could be indexed to the (101), (110), (004), (200), (105), (211), (204), (215), (224) planes of a combination of the anatase and rutile forms of TiO<sub>2</sub>,<sup>[31]</sup> with the rutile form showing relatively low intensity. This is in agreement with the standard XRD data (JCPDS 21-1272 and JCPDS 21-1276) (Figure S1) as well as those observed in the literature.<sup>[32,33]</sup> The typical diffraction peaks corresponding to Au and Pd were not observed for Au–TiO<sub>2</sub> and Pd–TiO<sub>2</sub> respectively due to their low concentration and small particle size. The XRD spectrum of NiFe-LDH shows peaks, which correspond to (003), (006), (012), (015), (018), (110) and (113) reflections of (no space here)NiFe hydroxalcite layered structure as indicated in the XRD data (JCPDS 40-0215) and supported by literature.<sup>[28]</sup> In contrast, the XRD pattern of CuFe-LDH indicates the presence of an LDH altered structure. CuFe-LDH shows two strong diffraction peaks at 35.5 and 38.7, which corresponds to the 311 and 111 planes of Fe<sub>2</sub>O<sub>3</sub> and CuO, respectively. This is consistent with the literature reported on the formation of calcined CuFe-LDH materials.<sup>[34,35]</sup>

The ATR-FTIR spectra of as-synthesized catalysts is shown in Figure 2. Au–TiO<sub>2</sub> and Pd–TiO<sub>2</sub> shows a broad band between 3000  $\text{cm}^{-1}$  and 3700  $\text{cm}^{-1}$  from the O–H stretching mode of absorbed water. The band at 1635  $\text{cm}^{-1}$  corresponds to the O–H bending vibration of absorbed water.<sup>[36]</sup> The band at 823  $\text{cm}^{-1}$  has been attributed to tetrahedral Ti–O stretching.<sup>[37]</sup> The peaks at 511  $\text{cm}^{-1}$  and 611  $\text{cm}^{-1}$  are characteristic titanium peaks indicating the lattice vibration of Ti–O–Ti network.<sup>[38]</sup>

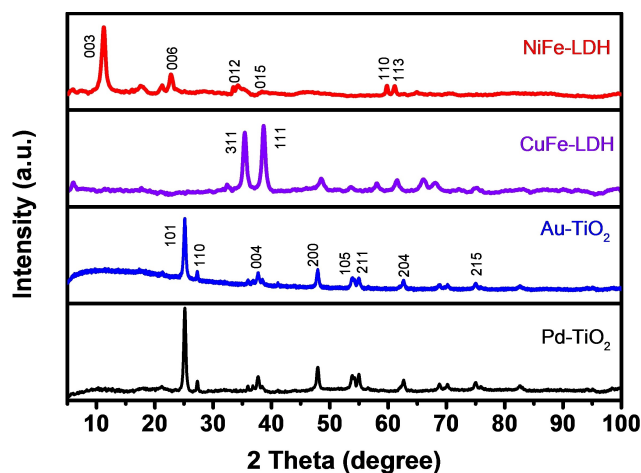


Figure 1. XRD patterns of as-synthesized catalyst materials.

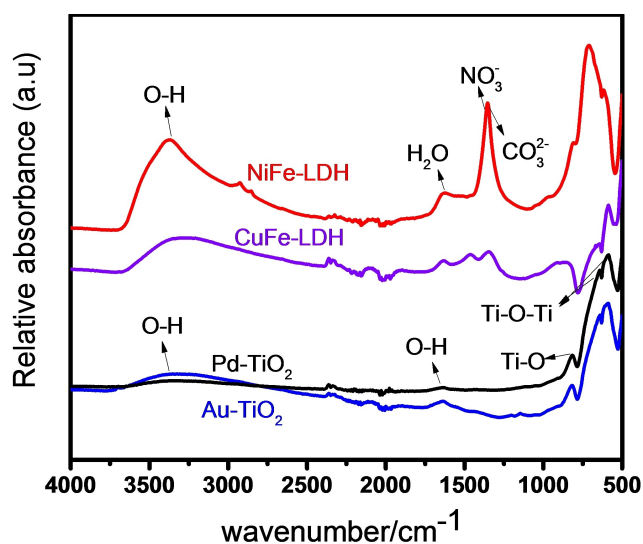


Figure 2. ATR-FTIR pattern of as-synthesized catalyst materials.

NiFe-LDH and CuFe-LDH exhibited the characteristic bands at  $3397\text{ cm}^{-1}$ , which is attributed to the O–H stretching vibration and  $1632\text{ cm}^{-1}$  which confirms the presence of interlayer water molecules. The peaks at  $1356\text{ cm}^{-1}$  and  $1373\text{ cm}^{-1}$  are attributed to interlayer carbonate and nitrate. Additional bands appeared between  $800\text{ cm}^{-1}$  and  $500\text{ cm}^{-1}$  which can be attributed to metal-oxygen (M–O) or metal-hydroxyl (M–OH) vibrations of LDH.<sup>[39]</sup>

The XPS analysis was conducted to derive information on the electronic state of all metal components in the catalytic materials. The XPS full survey data for monometallic Au–TiO<sub>2</sub> and Pd–TiO<sub>2</sub> are present in Figure 3. They show the electronic state of Au, Pd, and Ti. Where Ti results from TiO<sub>2</sub>, O from TiO<sub>2</sub>, Pd and Au was obtained from the precursors while C is obtained from the instrument. In the Au 4f core spectrum of Au–TiO<sub>2</sub> (Figure S2b), Au 4f<sub>5/2</sub> and Au 4f<sub>7/2</sub> were detected at a binding energy of 87.1 eV and 83.6 eV respectively which can

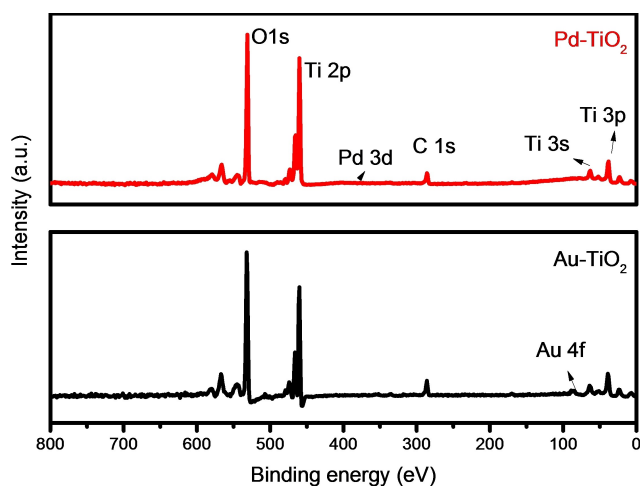


Figure 3. XPS survey scan for Au–TiO<sub>2</sub> and Pd–TiO<sub>2</sub>.

be attributed to metallic gold at zero-valent state (Au<sup>0</sup>).<sup>[29]</sup> The lower binding energy of Au 4f<sub>7/2</sub> as compared with the bulk Au values (Au 4f<sub>7/2</sub> at 84.0 eV) can be attributed to a strong interaction between Au and the oxygen vacancies of TiO<sub>2</sub>.<sup>[40]</sup> In the Pd 3d core spectrum of Pd–TiO<sub>2</sub> (Figure S2a), two well-defined peaks were observed; a high energy peak at 340.0 eV corresponding to Pd 3d<sub>3/2</sub> and a low energy peak at 334.8 eV corresponding to Pd 3d<sub>5/2</sub>.<sup>[41]</sup> The two weaker peaks located at 336.7 eV and 341.6 eV correspond to Pd<sup>2+</sup> 3d<sub>5/2</sub> and Pd<sup>2+</sup> 3d<sub>3/2</sub>. The theoretical peak position of metallic Pd (Pd<sup>0</sup>) is 335.1 eV and positive shift with respect to Pd<sup>0</sup> can be attributed to cationic species (Pd<sup>x</sup> with X ≥ 2) and or Pd/PdO<sub>x</sub> interface.<sup>[42]</sup> Hence the XPS information of Pd 3d suggests that Pd existed in the (0) and (+2) chemical state.<sup>[43]</sup> Generally, Pd<sup>0</sup> metal nanoparticles tend to form a thin layer of PdO around the particles to stabilize themselves, when they are exposed to air. This is supported by literature that suggests the existence of Pd nanoparticles as Pd<sup>0</sup> core and Pd<sup>2+</sup> shell. This is a clear indication that Pd–TiO<sub>2</sub> is easily oxidized. The O 1s spectra of both catalysts (Au–TiO<sub>2</sub> and Pd–TiO<sub>2</sub>) are represented in (Figure S2d). Two peaks located at ≈530.4 eV and ≈531. eV are visible and were assigned to the Ti–OH bond and Ti–O–O.<sup>[45]</sup> A blue shift is observed in the binding energies of O 1s of Pd–TiO<sub>2</sub> than Au–TiO<sub>2</sub> which may result from a stronger interaction in Pd–TiO<sub>2</sub> catalyst. The Ti 2p spectrum of Au–TiO<sub>2</sub> and Pd–TiO<sub>2</sub> are represented (Figure S2c). The Ti 2p spectrum corresponds to two peaks, the Ti 2p<sub>3/2</sub> at ≈459.2 eV and Ti 2p<sub>1/2</sub> at ≈464.3 eV, which is assigned to titanium in the IV oxidation state.<sup>[46]</sup> The spectrum also shows a peak at ≈458.6 eV which corresponds to Ti<sup>3+</sup>. Compared to Au–TiO<sub>2</sub>, the binding energy values of Ti 2p of Pd–TiO<sub>2</sub> shifts to a higher value, which is a clear indication that there is a stronger interaction between Pd and TiO<sub>2</sub> than Au and TiO<sub>2</sub>.

The XPS full survey scan of LDH materials (CuFe-LDH and NiFe-LDH) was extensively investigated and displayed in Figure 4. The spectra indicates the presence of Ni, Fe, Cu, C and O. The O 1s and C 1s peaks have low intensities, which suggests that surface oxidation and contamination are relatively low. The

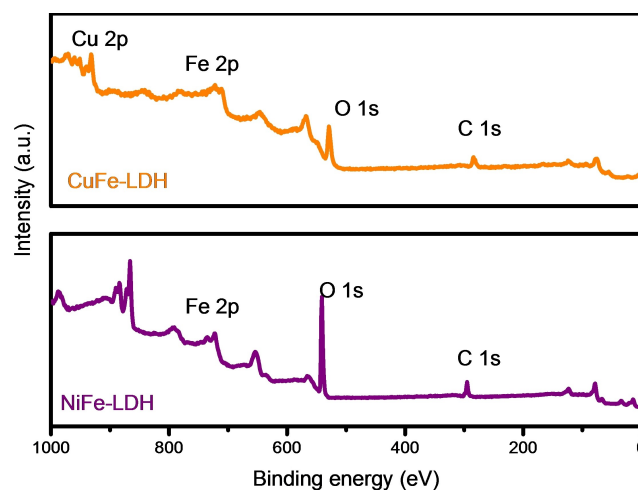


Figure 4. XPS survey scan for NiFe-LDH and CuFe-LDH.

high-resolution spectrum of Ni 2p (Figure S3b) shows two main peaks at 855.7 eV and 873.2 eV which can be attributed to Ni 2p<sub>1/2</sub> and Ni 2p<sub>3/2</sub> respectively. A shakeup satellite at 861.3 eV is also observed which is a characteristic of the element Ni in the +2 valence state<sup>[47]</sup> and +3 valence state. The core-level spectrum of Cu 2p (Figure S3a) shows two peaks at 951.50 and 931.73 eV which corresponds to Cu 2p<sub>1/2</sub> and Cu 2p<sub>3/2</sub>. Two other satellite peaks located at 960.46 and 939.70 eV were also observed for Cu 2p which indicates the presence of copper with a 3d<sup>9</sup> outermost electron configuration.<sup>[48]</sup> The core-level spectrum of Fe 2p for NiFe-LDH and CuFe-LDH is represented in (Figure S2c). Two peaks at 724.90 and 711.59 eV were observed on NiFe-LDH which corresponds to the Fe 2p<sub>1/2</sub> and Fe 2p<sub>3/2</sub>. These represent the presence of iron oxide and hydroxide species.<sup>[49]</sup> For CuFe-LDH, the Fe 2p<sub>1/2</sub> was located at 722.29 eV and the Fe 2p<sub>3/2</sub> exhibited of two split peaks at 717.04 and 711.09 eV indicating that iron in CuFe-LDH corresponds to Fe<sup>3+</sup> oxidation state.<sup>[50]</sup>

The TEM analysis of Au–TiO<sub>2</sub> and Pd–TiO<sub>2</sub> are shown in Figure 5 and 6, respectively. Small/thick dark (opaque) spots with clear boundary can be seen on the surface of more bright/transparent/large sized particles. This dark/bright contrast is a

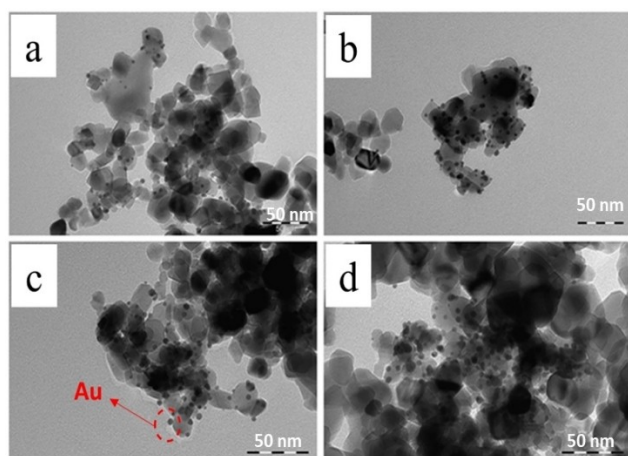


Figure 5. TEM images of 1% Au–TiO<sub>2</sub>.

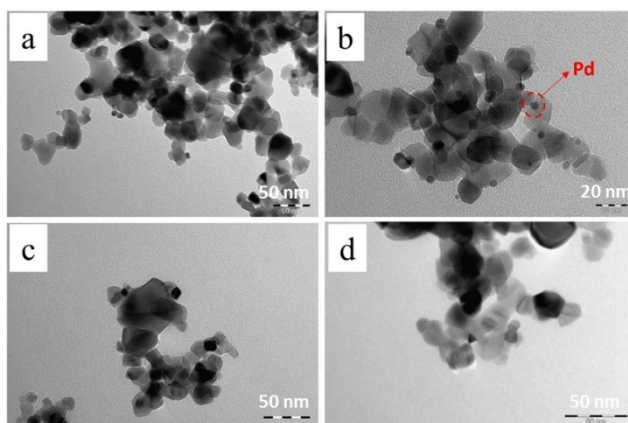


Figure 6. TEM images of 1% Pd–TiO<sub>2</sub>.

clear indication of the difference in atomic number of the elements present in Figure 5 and 6. The lower atomic number (TiO<sub>2</sub>) exhibits a bright spot, while the higher atomic numbers (Au, Pd) exhibits darker spots. This differentiates the decorated metal nanoparticles (Au, Pd) from the anchoring support (TiO<sub>2</sub>). The TEM image of Au–TiO<sub>2</sub> (Figure 5) also showed that well-controlled sizes of Au nanoparticles were homogeneously distributed across the TiO<sub>2</sub> crystal surfaces in uniform shapes, predominantly in spheres, with a possible mixture of cub-octahedral, decahedral, and icosahedral shaped particles (HAADF-STEM), as reported in our previous work.<sup>[23,25]</sup> The average particle size of AuNPs was calculated as 3–5 nm using image J software.

Figure 6 shows the TEM images of Pd–TiO<sub>2</sub>. The Pd nanoparticles were sparsely distributed on the TiO<sub>2</sub> surface. The Pd nanoparticles were a mixture of spherical and trigonal shaped particles, with the spherical shaped particles existing predominantly while the trigonal particles exist rarely. The particle size ranged from 4–8 nm.

SEM images show that NiFe-LDH (Figure 7a, b) crystals were formed and the particles were almost uniform in shape and size. They exhibited exclusively hexagonal platelet like structures with sharp boundaries (Figure 7c, d) which can be clearly seen from the images. The presence of Ni, Fe elements were cross checked by EDX while scanning and confirmed their presence.

The SEM images of CuFe-LDH (Figure 8 a, b) exhibited hexagonal shaped particles with sharp edges and they were stacked on each other which is evident from dark field and bright field images. The CuFe-LDH particles were thin enough for the electron beam to penetrate and reveal their shape. However, Figure 8 c and d reveal the agglomeration of the CuFe-LDH particles. The average diameter of the particles was approximately 100 nm. Again, this is a characteristic nature of LDH crystal formation. The presence of Cu, Fe elements was also confirmed by EDX.

To determine the exact percentage of Au and Pd in (1%) Au–TiO<sub>2</sub> and (1%) Pd–TiO<sub>2</sub>, ICP-OES analysis was performed. The results confirmed the presence of Au and Pd in our catalyst

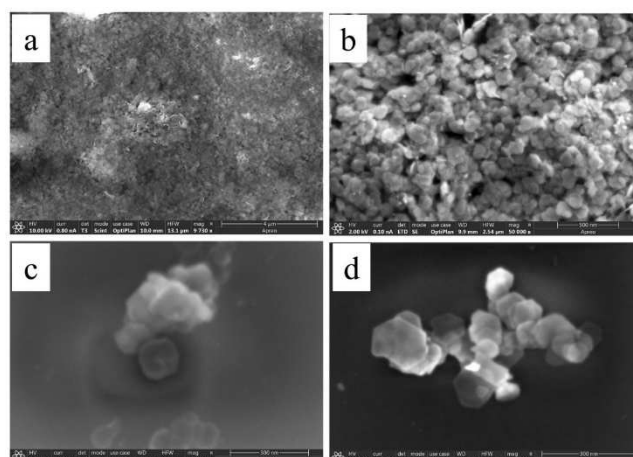
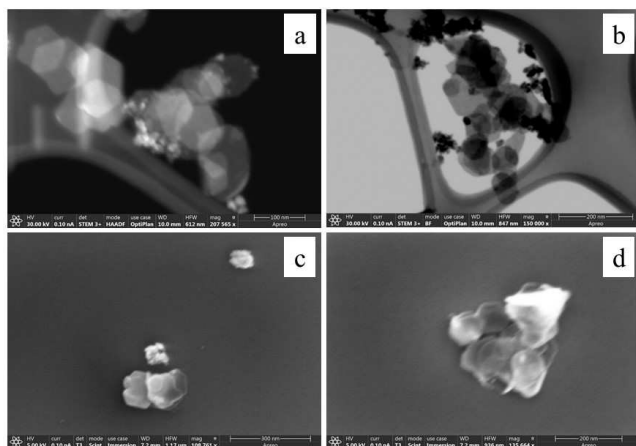


Figure 7. SEM images of NiFe-LDH. Scale: a) 4 μm, b) 500 nm, c&d) 300 nm.



**Figure 8.** SEM images of CuFe-LDH. Scale: a) 100 nm, b&d) 200 nm, c) 300 nm.

samples. The quantitative determination of Au was found to be 2.42 ppm (Theoretical Au content: 2.44 ppm). This means that the theoretical 1% loading of Au on TiO<sub>2</sub> is the same 1% experimentally. Thus the immobilization of Au colloid on TiO<sub>2</sub> was confirmed to be 100% successful and efficient.

However, the ICP-OES measurement of Pd–TiO<sub>2</sub> showed that only 0.7266 ppm of Pd was present in the sample solution instead of 2.44 ppm. It was an alarming indication that Pd colloid immobilization on TiO<sub>2</sub> was only 30% successful. In reality, it may not be the case. Because during material synthesis, Pd colloid (dark brown in colour) immobilization on TiO<sub>2</sub> was ~100% successful which was evident from the colourless filtrate. We believe that a large amount of Pd<sup>(0)</sup> metal was converted into PdO precipitate upon the harsh pre-treatment with HNO<sub>3</sub>/HCl mixture during metal extraction, which led to incomplete dissolution of the catalyst material (1% Pd–TiO<sub>2</sub>). These PdO solid particles might have been filtered off from the solution before aspirating the solution in flame.; Hence a major difference was observed between the theoretical value (2.42 ppm) and the experimental value (0.7266 ppm). Same scenario was encountered when the material was dissolved hydrothermally. The theoretical 1% Pd–TiO<sub>2</sub> should also have 1% Pd experimentally, but it is undetectable due to its conversion into an insoluble oxide form.

### Electrochemical reduction of 4-NP on TiO<sub>2</sub> supported nanoparticles

The electrocatalytic behaviour of bare GCE and catalyst modified GCE electrodes (Pd–TiO<sub>2</sub> and Au–TiO<sub>2</sub>) in the presence and absence of 1 mM 4-NP using cyclic voltammetry at a scan rate of 50 mV/s is shown in Figure 9a. The results show that bare GCE and Pd–TiO<sub>2</sub> in the absence of 4-NP shows no electrochemical activity in the absence of 4-NP. The CV of Au–TiO<sub>2</sub> shows a single redox couple in the absence of 4-NP which can be attributed to atmospheric moisture. The introduction of 4-NP (1 mM) into the electrochemical cell resulted in the

appearance of two redox pairs on bare GCE. The first redox pair observed at –0.81 V is attributed to the formation of the radical anion (Scheme 1, step 1) and the second redox pair observed at –1.71 V is assigned to the formation of the dianion (Scheme 1, step 2). Similar results have been reported previously for the electrochemical activity of phenols and quinones on bare GCE in organic solvent.<sup>[51]</sup> This observed activity of GCE is as a result of the oxygenated functional groups present on the GCE surface which sometimes promotes electron transfer in non-aqueous solvents.<sup>[52]</sup>

To the best of our knowledge, there have been only two reaction mechanisms for 4-NP reduction reaction reported. They are mainly dependent on the adsorption of 4-NP on the catalyst surface followed by intra/inter molecular electronic transitions and protonation. These reaction paths differ based on the electrode, solvent, electrolyte and difference in catalytic active sites. We believe that the adsorption of 4-NP on Au–TiO<sub>2</sub> and Pd–TiO<sub>2</sub> catalysts was just a physisorption followed by stepwise reduction of –NO<sub>2</sub> to –NO. On the contrary, the self-polarized –O–N=O group in 4-NP molecules were chemisorbed on the brucite (metal cations) layers of LDH followed by its reduction.<sup>[26–28]</sup>

Six electrochemical events were observed on Au–TiO<sub>2</sub> and Pd–TiO<sub>2</sub> for the reduction of 4-NP: three reduction peaks (R<sub>i</sub>, R<sub>ii</sub>, R<sub>iii</sub>) and three oxidation peaks (O<sub>i</sub>, O<sub>ii</sub>, O<sub>iii</sub>). These peaks increased tremendously compared to bare GCE because of a higher adsorption of 4-NP on Au–TiO<sub>2</sub> and Pd–TiO<sub>2</sub> surface, which enhances the electrochemical activity of 4-NP. On Pd–TiO<sub>2</sub>, the electrocatalytic reduction of 4-NP started at an onset potential of –0.32 V and provides three cathodic peaks positioned at –0.95 V (R<sub>i</sub>), –1.33 V (R<sub>ii</sub>) and –1.85 V (R<sub>iii</sub>). While on Au–TiO<sub>2</sub>, the electrocatalytic reduction of 4-NP started at an onset potential of –0.61 V with cathodic peaks positioned at –0.75 V (R<sub>i</sub>), –1.01 V (R<sub>ii</sub>) and –1.88 V (R<sub>iii</sub>). The chemically irreversible double wave (R<sub>i</sub> and R<sub>ii</sub>) observed can be attributed to the reduction of 4-NP to its radical anion as a result of a self-protonation process. This is consistent with those previously reported in the literature on the reduction of 4-NP in non-aqueous solvent.<sup>[54]</sup>

R<sub>iii</sub> is a chemically reversible peak observed at an onset potential of –1.45 V and –1.63 V on Pd–TiO<sub>2</sub> and Au–TiO<sub>2</sub> respectively. A corresponding oxidative peak (O<sub>iii</sub>) for R<sub>iii</sub> was formed at –1.77 V and –1.81 V on Pd–TiO<sub>2</sub> and Au–TiO<sub>2</sub>. R<sub>iii</sub> corresponds to the peak observed for the reduction of 4-nitrophenolate anion, a product formed as a result of the double wave (R<sub>i</sub> and R<sub>ii</sub>). According to Amatoore et al.<sup>[55]</sup> the final products of the reduction of 4-NP in DMSO is 4-aminiphenol (4-AP) and the 4-nitrophenolate anion. This was also supported by Farnia et al.<sup>[56]</sup> All corresponding data for the reduction 4-NP are shown in Table 1. Comparing the electrocatalytic activity of Au–TiO<sub>2</sub> and Pd–TiO<sub>2</sub>, it is observed that Pd–TiO<sub>2</sub> shows a slightly reduced potential for the electroreduction of 4-NP. Although, it was observed that Au–TiO<sub>2</sub> had a smaller particle size (3–5 nm), than Pd–TiO<sub>2</sub> (4–8 nm) as confirmed by TEM (Figure 5 and 6). The improved electrocatalytic activity of Pd–TiO<sub>2</sub> could be due to a higher binding energy value of Ti 2p<sub>3/2</sub> and a possible Pd<sup>0</sup>/Pd<sup>2+</sup> bivalent core

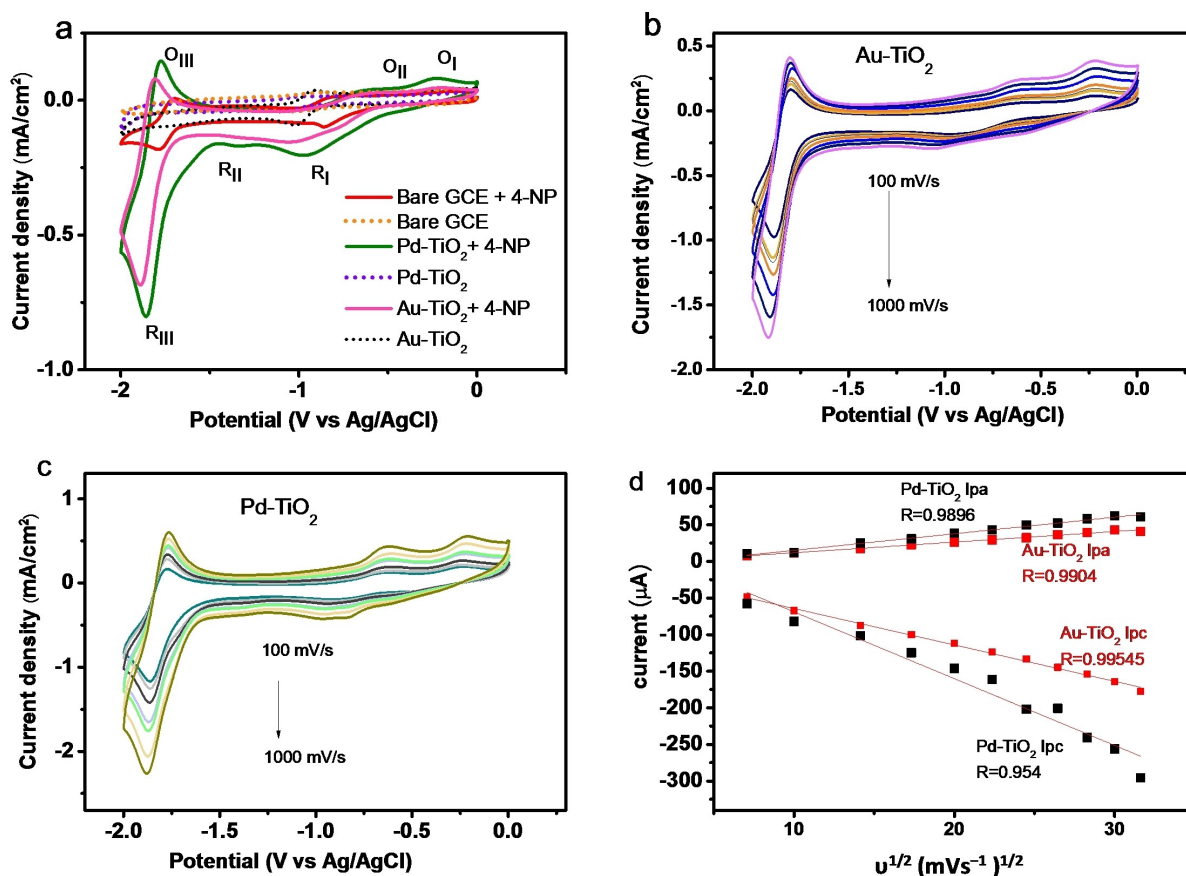


Figure 9. a) Bare and modified GCE with 4-NP (solid lines) and without 4-NP (dotted lines) in 0.1 M TBAPF<sub>6</sub> and b,c) CV scans of Au-TiO<sub>2</sub> and Pd-TiO<sub>2</sub> at different scan rates ranging from 100–1000 mV s<sup>-1</sup>. d) Corresponding cathodic and anodic peak values Vs square root of scan rate.

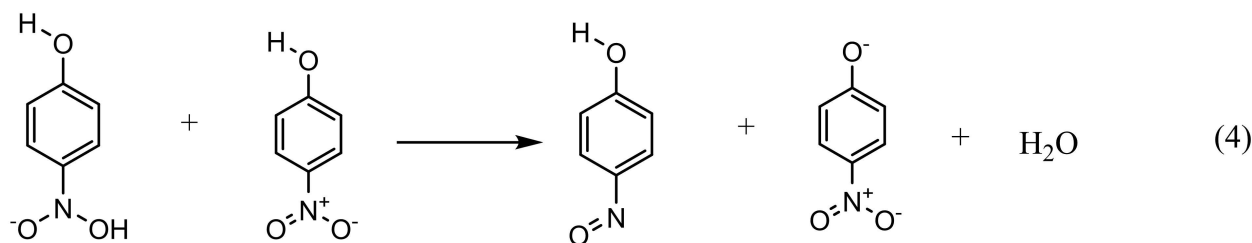
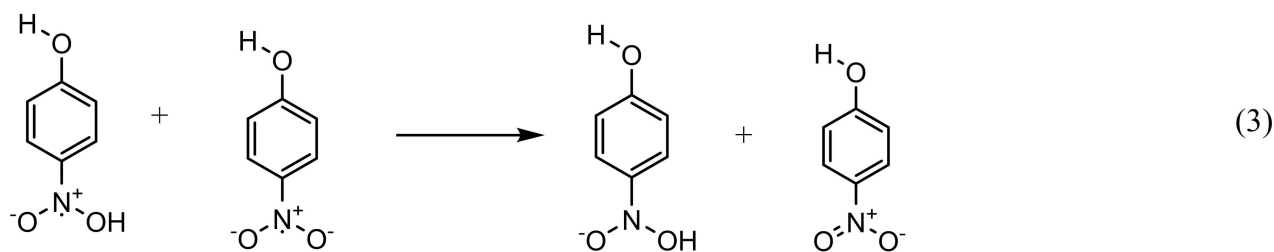
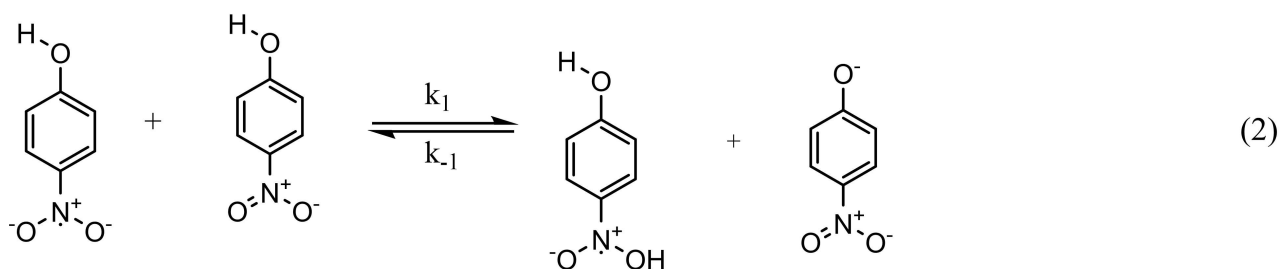
**Table 1.** Cyclic Voltammetric data of reduction onset (\*) and peak position (\*\*\*) of 4-NP (1 mM) reduction in 0.1 M TBAPF<sub>6</sub>/ACN on different modified GCE at a scan rate of 50 mV/s. The potentials are vs Ag/AgCl.

GCE electrode	Reduction onset(*) [V]	R <sub>I</sub> (**) [V]	R <sub>II</sub> (**) [V]	R <sub>III</sub> (*) [V]	R <sub>III</sub> (**) [V]	O <sub>III</sub> (**) [V]	O <sub>II</sub> (**) [V]	O <sub>I</sub> (**) [V]
Pd-TiO <sub>2</sub>	-0.32	-0.95	-1.33	-1.47	-1.85	-1.77	-0.58	-0.23
NiFe-LDH	-0.56	-0.69	-1.10	-1.49	-1.88	-1.76	-0.42	-0.14
CuFe-LDH	-0.93	-	-1.22	-1.57	-1.87	-1.76	-0.67	-0.13
Au-TiO <sub>2</sub>	-0.61	-0.75	-1.01	-1.64	-1.88	-1.81	-0.55	-0.22

shell structure, which is formed upon Pd oxidation, so the active site may not be fully Pd<sup>0</sup>, but Pd<sup>0</sup>/Pd<sup>2+</sup> couple. This is not the case with AuNPs, as they have shown clear characteristic Au<sup>0</sup> binding energy, as observed by XPS (Figure S2b). We have also inferred from our previous works that when the Pd<sup>0</sup> metal NPs is immobilized on TiO<sub>2</sub>, the NPs will wet the surface of the TiO<sub>2</sub> like a water droplet wets the paper surface and loses its structure/shape slightly.<sup>[57]</sup> Whereas, AuNPs stay stable on the TiO<sub>2</sub> surface without losing its structure. This wetting behaviour observed on Pd-TiO<sub>2</sub> is facilitated by Pd's oxygen affinity, thereby creating Pd↔TiO<sub>2</sub> interstitial sites. These metal↔support interstitial sites coupled with the freely exposed Pd metal atoms, contributes to the improved electrocatalytic performance of Pd-TiO<sub>2</sub> over Au-TiO<sub>2</sub>. Therefore the combination of 1) freely exposed surface metal atoms of NPs and 2) metal↔support interstitial sites together contribute in the catalytic

activation of 4-NP. In case of Pd, both these factors play the role in catalytic activity. For Au, it is the freely exposed surface metal atoms. As the nature of the catalytic active sites are different in Au-TiO<sub>2</sub> and Pd-TiO<sub>2</sub>, we see difference in 4-NP electro-reduction performance.

The oxidative peaks O<sub>I</sub>, O<sub>II</sub> and O<sub>III</sub> observed on the anodic sweep of Pd-TiO<sub>2</sub> and Au-TiO<sub>2</sub> were positioned at a potential of ≈ -0.30 V, ≈ -0.60 V and ≈ -1.90 V correspond to the oxidation of products formed during the cathodic reduction (4-hydroxylaminophenol and 4-nitrophenolate anion).<sup>[53]</sup> The influence of different scan rates on the reduction and oxidation response of 1 mM 4-NP in 0.1 M TBAPF<sub>6</sub> and ACN using Au-TiO<sub>2</sub> and Pd-TiO<sub>2</sub> catalysts was studied (Figure 9b and 9c). A consistent increase in the oxidation and reduction peaks with increasing scan rate was observed for both Au-TiO<sub>2</sub> and Pd-TiO<sub>2</sub>. The anodic and cathodic peak current (lpa and lpc) for



Scheme 1. Mechanism for the reduction of 4-NP in aprotic solvent.<sup>[53]</sup>

4-NP shows a linear relationship with the square root of scan rates (Figure 9d), indicating that both oxidation and reduction of 4-NP follow a diffusion controlled process.<sup>[58]</sup> The linear relationship also proves that the fabrication of the catalyst material was stable and no leaching was observed from the electrode surface during CV cycles (Figure 9d).

#### Electrochemical reduction of 4-NP on LDH catalysts

The electrocatalytic behaviour of bare and modified (CuFe-LDH and NiFe-LDH) GCE electrodes in the presence and absence of 1 mM 4-NP using CV is shown in Figure 10a. No redox peaks were observed at bare and modified GCE surfaces without 4-NP, which implies that the materials are electrocatalytically inactive

in the potential window. Upon the introduction of 1 mM 4-NP, CuFe-LDH and NiFe-LDH modified GCE shows a shift in reduction peak potential with higher current as compared to bare GCE. Different electrochemical events were observed on CuFe-LDH and NiFe-LDH, these are similar to those observed on the TiO<sub>2</sub> supported monometals (Pd-TiO<sub>2</sub> and Au-TiO<sub>2</sub>) in Figure 9a. Three reduction peaks (R<sub>i</sub>, R<sub>ii</sub>, R<sub>iii</sub>) and three oxidation peaks (O<sub>i</sub>, O<sub>ii</sub>, O<sub>iii</sub>) were observed. The obtained reduction peak potential are as follows: on NiFe-LDH, the electrocatalytic reduction of 4-NP started at an onset potential of -0.56 V with cathodic peaks positioned at -0.69 V (R<sub>i</sub>), -1.10 V (R<sub>ii</sub>) and -1.88 V (R<sub>iii</sub>). While on CuFe-LDH the electrocatalytic reduction of 4-NP started at an onset potential of -0.93 V. The double wave (R<sub>i</sub> and R<sub>ii</sub>) which is attributed to the self-protonation process of 4-NP to its radical anion<sup>[53]</sup> is summed into a sharp, well-defined



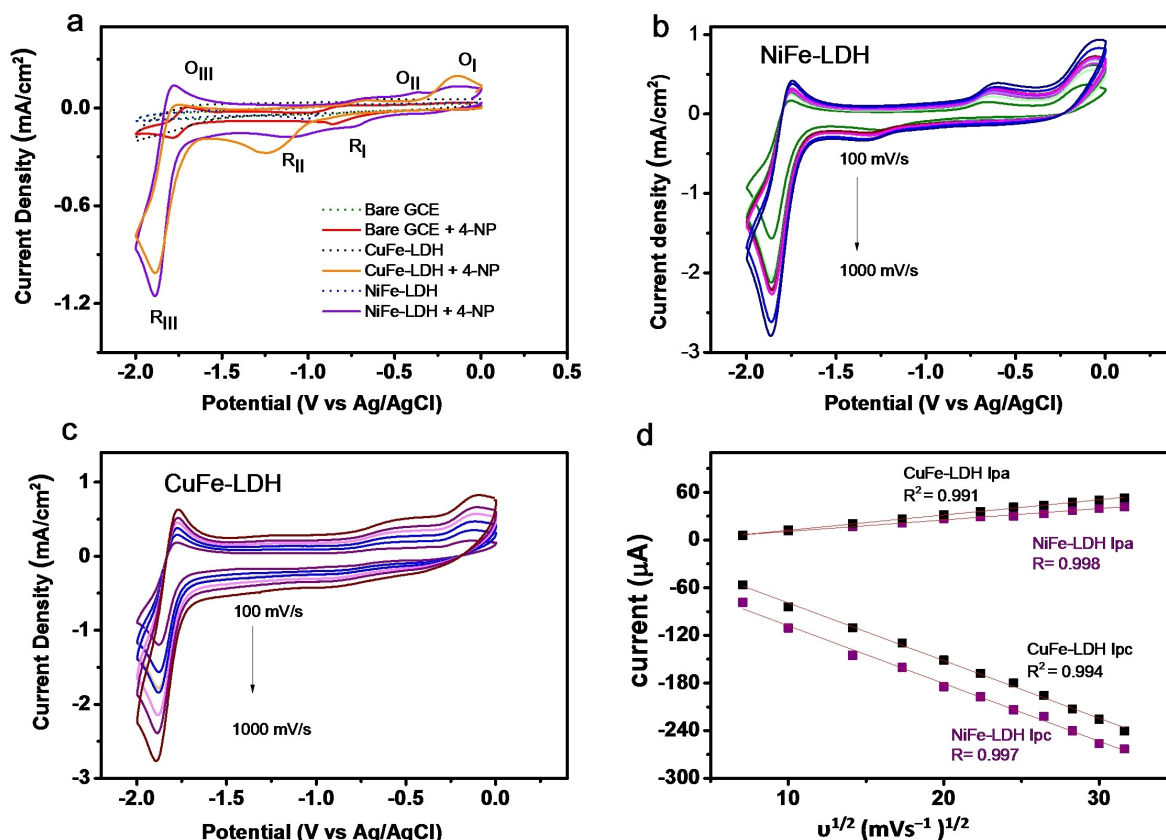


**Figure 10.** a) Bare GCE, CuFe-LDH and NiFe-LDH modified electrode with and without 4-NP in 0.1 M TBAPF<sub>6</sub> and b,c) CV of NiFe-LDH and CuFe-LDH at different scan rates ranging from 10–1000 mV s<sup>-1</sup>. d) Ip Vs square root of scan rate ( $u^{1/2}$ ).

peak, positioned at  $-1.22$  V. The third reduction peak ( $R_{III}$ ) was observed with an onset potential of  $-1.57$  V and a clear peak was positioned at  $-1.87$  V. The oxidative peaks  $O_I$ ,  $O_{II}$  and  $O_{III}$  positioned at a potential of  $\approx -0.15$  V,  $-0.68$  V and  $\approx -1.78$  V on CuFe-LDH and NiFe-LDH, correspond to the oxidation of products formed during the cathodic reduction (4-hydroxylaminophenol and 4-nitrophenolate anion) as reported by Silvester et al.<sup>[53]</sup> All corresponding data for the reduction of 4-NP on CuFe-LDH and NiFe-LDH are listed in Table 1. From results obtained, it is evident that NiFe-LDH shows a slightly less negative reduction potential as compared to CuFe-LDH. This was attributed to the aggregation of the CuFe-LDH particles, which results in a decrease of catalytically active centres on CuFe-LDH surface and then causes a decline in its activity towards 4-NP reduction.

A comparison of our synthesized materials with those already reported by literature for 4-NP electrocatalysis in aprotic solvent is shown in Table 2. Our materials show superiority in terms of a lower reduction potential for reduction peaks  $R_I$ ,  $R_{II}$  and  $R_{III}$ . Forryan et al. also reported three reduction peaks,  $R_I$ ,  $R_{II}$  and  $R_{III}$  at  $-1.02$  V,  $-1.53$  V and  $-1.92$  V vs. Ag<sup>[59]</sup> respectively. Silvester et al. reported a slightly lower reduction potential for  $R_{III}$  at  $-1.79$  V vs. Ag, this could be as a result of difference in viscosity and diffusion of ionic liquids<sup>[53]</sup> as compared to acetonitrile which was used in this work. Although we cannot compare our results directly to reported methods as the combination of material, electrode, electrolyte and solvent varies, the benchmark catalyst can be assessed in terms that are more general. Other reports that claim high efficiency for 4-NP reduction catalysis used reductants like NaBH<sub>4</sub> and high-energy radiation like UV rays. A recent report where Ag was immobi-

**Table 2.** Summary of literature results reported for reduction of 4-NP in aprotic solvent.

Electrode /Catalyst Material	Electrolyte	$R_I$ [V]	$R_{II}$ [V]	$R_{III}$ [V]	Reference
Gold	[C <sub>4</sub> dmim][N(Tf) <sub>2</sub> ]	$-1.03$ Vs. Ag	$-1.31$ Vs. Ag	$-1.79$ Vs. Ag	[53]
Gold	0.2 M TBAP/ DMF	$-1.02$ Vs. Ag	$-1.53$ Vs. Ag	$-1.92$ Vs. Ag	[59]
Pd–TiO <sub>2</sub>	0.1 M TBAPF <sub>6</sub> /ACN	$-0.95$ Vs. Ag/AgCl	$-1.33$ Vs. Ag/AgCl	$-1.85$ Vs. Ag/AgCl	Present work
NiFe-LDH	0.1 M TBAPF <sub>6</sub> /ACN	$-0.69$ Vs. Ag/AgCl	$-1.10$ Vs. Ag/AgCl	$-1.88$ Vs. Ag/AgCl	Present Work
CuFe-LDH	0.1 M TBAPF <sub>6</sub> /ACN	–	$-1.22$ Vs. Ag/AgCl	$-1.87$ Vs. Ag/AgCl	Present work
Au–TiO <sub>2</sub>	0.1 M TBAPF <sub>6</sub> /ACN	$-0.75$ Vs. Ag/AgCl	$-1.01$ Vs. Ag/AgCl	$-1.88$ Vs. Ag/AgCl	Present Work

lized on Co–Al LDH composed with poly (o-phenylenediamine) was shown to reduce 4-NP at a low potential ( $-0.3$  V vs SCE) in aqueous buffer environment.<sup>[9]</sup> Liguang et al. also reported a highly recyclable hybrid material, xCu-LDH/rGO, which catalyses  $\text{NaBH}_4$  mediated 4-NP reduction.<sup>[60]</sup> Haiqing et al. reported a Pd/CNT composite as highly efficient catalyst.<sup>[61]</sup> Under electrocatalytic conditions in aqueous solvent, a heterostructured composite containing  $\text{Fe}_3\text{O}_4/\text{ZnO}/\text{Fe}^0/\text{Fe}_3\text{C}/\text{g-C}$  calcined at  $900^\circ\text{C}$ , claimed to be a better catalyst with improved reduction of 4-NP in a recent report.<sup>[62]</sup> This complicated heterostructure material shows the reduction ability of 4-NP between  $+0.05$  V and  $-0.5$  V vs Ag. Our materials also stand close to these onset reduction potential range Pd– $\text{TiO}_2$  ( $-0.32$  V), NiFe-LDH ( $-0.56$  V), Au– $\text{TiO}_2$  ( $-0.61$  V) and CuFe-LDH ( $-0.93$  V).

Figure 10b and 10c shows the electrochemical reduction of 4-NP at different scan rates ranging from  $100$  to  $1000$   $\text{mVs}^{-1}$ . Similar to the  $\text{TiO}_2$  supported nanoparticles, the anodic and cathodic peak current ( $I_{pa}$  and  $I_{pc}$ ) increased linearly with the square root of scan rates (Figure 10d). This is a clear indication that the oxidation and reduction of 4-NP on both CuFe-LDH and NiFe-LDH follows a diffusion controlled process.

A comparison of the CV response of catalyst materials for the electro-reduction of 4-NP is represented in Figure 11. By comparing all GCE modified electrodes to bare GCE, it was observed that all catalyst materials in this study, exhibit enhanced performance towards electrocatalytic reduction of 4-NP. The voltammograms displayed a similar shape for all materials studied: with three reduction peaks and three oxidation peaks. All synthesized catalysts displayed a well-defined reduction peak ( $R_{III}$ ) with an onset potential of  $-0.32$  V,  $-0.56$  V,  $-0.61$  V,  $-0.93$  V and for Pd– $\text{TiO}_2$ , NiFe-LDH, Au– $\text{TiO}_2$ , and CuFe-LDH respectively. Of all the materials studied, Pd– $\text{TiO}_2$  showed the best result for electrocatalytic reduction of 4-NP with a much lower onset potential of  $-0.32$  V. This is due to (i) an improved synergistic interaction between  $\text{Pd}^0/\text{Pd}^{2+}$  core and  $\text{TiO}_2$  (observed by the binding energy values) and (ii) a wetting behaviour facilitated by Pd's oxygen affinity which creates Pd

$\leftrightarrow\text{TiO}_2$  interstitial sites. Therefore, the electrocatalytic reduction of 4-NP in TBAPF<sub>6</sub>/ACN follows the order: Pd– $\text{TiO}_2$  > NiFe-LDH > Au– $\text{TiO}_2$  > CuFe-LDH.

## Conclusions

In this paper, we have developed and characterized catalysts for the electrochemical reduction of 4-NP in  $0.1$  M TBAPF<sub>6</sub> and ACN. The physicochemical and electrochemical properties of all catalysts (Pd– $\text{TiO}_2$ , Au– $\text{TiO}_2$ , CuFe-LDH and NiFe-LDH) were studied and reported in detail. To the best of our knowledge, there has been no literature reports on the electrocatalytic investigation of Ni–Fe, Cu–Fe couples in non-aqueous conditions using a polar aprotic solvent (ACN) and TBAPF<sub>6</sub> as electrolyte. Therefore, the catalytic activity of LDHs reported in literature is not directly comparable with our work due to the difference in reaction conditions: concentration of 4-NP, choice of electrodes, electrolytes, solvent system and applied potential range. These conditions have a huge impact on the results obtained. Hence the comparison is merely qualitative than quantitative.

Our results showed that the extent of electrochemical reduction of 4-NP was dependent on the nature of the electrode material. Difference in reduction potential and current response was noted along the series of catalysts (Pd– $\text{TiO}_2$ , Au– $\text{TiO}_2$ , CuFe-LDH and NiFe-LDH) showing that all catalysts were suitable for the electroreduction of 4-NP. An initial self-protonation reaction was observed followed by a reaction with the parent molecule to form a radical species, which underwent further electrochemical reductions until 4-AP was formed. Pd– $\text{TiO}_2$  showed the lowest overpotential for  $R_{III}$  at an onset of  $-0.32$  V with a well-defined peak, positioned at  $-1.85$  V. The presence of  $\text{Pd}^0/\text{Pd}^{2+}$  active site,  $\text{Pd}\leftrightarrow\text{TiO}_2$  interstitial sites and the freely exposed Pd metal atom, together aids in enhancing Pd– $\text{TiO}_2$  electrocatalytic activity. The catalytic activity followed the order Pd– $\text{TiO}_2$  > NiFe-LDH > Au– $\text{TiO}_2$  > CuFe-LDH. All catalysts showed a capacity to reduce 4-NP, which creates an opportunity to expand the electrocatalytic materials for further photoelectrochemical studies and other environmental remediation applications.

## Acknowledgements

A.O.K acknowledges: (i) University of Turku Graduate School (UTUGS) Doctoral Programme in Exact Sciences (EXACTUS), (ii) Real Estate Foundation and (iii) Business Finland (COMPOL project) for financial support. L.K thanks Turku Collegium for Science & Medicine (TCSM) and Finnish Cultural Foundation (SKA) for funding. We thank the Electron Microscopy Laboratory, Institute of Biomedicine, University of Turku and Biocenter Finland for the TEM analysis. Further, we thank the MATSURF consortium for SEM and XPS analysis.

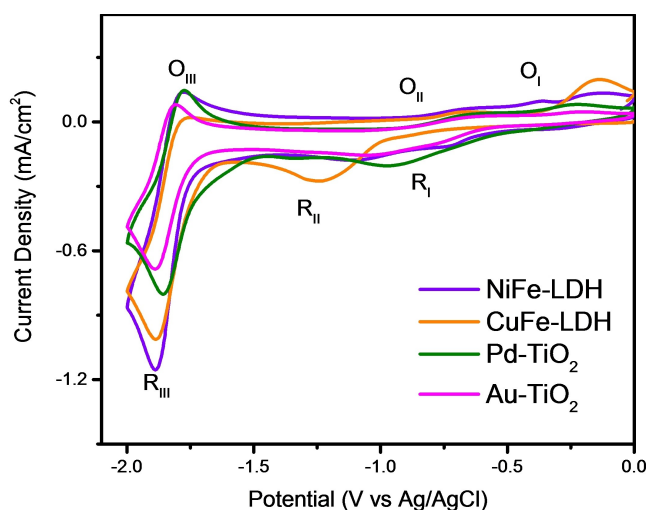


**Figure 11.** Comparison of the CVs of at a scan rate of  $50$   $\text{mVs}^{-1}$  in  $1$  mM 4-NP +  $0.1$  M TBAPF<sub>6</sub> in ACN.

## Conflict of Interest

The authors declare no conflict of interest.

## Data Availability Statement

The data that support the findings of this study are available from the corresponding author upon reasonable request.

**Keywords:** cyclic voltammetry · LDH · metal catalysts · nanocomposite · 4-nitrophenol · semiconductors

- [1] Z. YongChun, Q. YiTai, *Sci. China Ser. G Physics, Mech. Astron. Sci. China Ser. G-Phys Mech Astron* **2009**, *52*, 13–20.
- [2] M. Hussain, M. Ahmad, A. Nisar, H. Sun, S. Karim, M. Khan, S. D. Khan, M. Iqbal, S. Z. Hussain, *New J. Chem.* **2014**, *38*, 1424–1432.
- [3] H. Rodríguez Molina, J. L. Santos Muñoz, M. I. Domínguez Leal, T. R. Reina, S. Ivanova, M. Á. Centeno Gallego, J. A. Odriozola, *Front. Chem.* **2019**, *7*, 548.
- [4] K. Edalati, Q. Wang, H. Eguchi, H. Razavi-Khosroshahi, H. Emami, M. Yamauchi, M. Fuji, Z. Horita, *Mater. Res. Lett.* **2019**, *7*, 334–339.
- [5] H. Maltanova, S. Poznyak, M. Starykevich, M. Ivanovskaya, *Electrochim. Acta* **2016**, *222*, 1013–1020.
- [6] G. Mishra, B. Dash, S. Pandey, *Appl. Clay Sci.* **2018**, *153*, 172–186.
- [7] C. Li, M. Wei, D. G. Evans, X. Duan, *Small* **2014**, *10*, 4469–4486.
- [8] M. L. Di Vona, M. Casciola, A. Donnadio, M. Nocchetti, L. Pasquini, R. Narducci, P. Knauth, *Int. J. Hydrogen Energy* **2017**, *42*, 3197–3205.
- [9] T. Dhanasekaran, R. Manigandan, A. Padmanaban, R. Suresh, K. Giribabu, V. Narayanan, *Sci. Rep.* **2019**, *9*, 1–17.
- [10] M. Zubair, M. Daud, G. McKay, F. Shehzad, M. A. Al-Harhi, *Appl. Clay Sci.* **2017**, *143*, 279–292.
- [11] N. Arora, A. Mehta, A. Mishra, S. Basu, *Appl. Clay Sci.* **2018**, *151*, 1–9.
- [12] H. Yin, Y. Zhou, S. Ai, Q. Ma, L. Zhu, L. Lu, *Int. J. Environ. Anal. Chem.* **2012**, *92*, 742–754.
- [13] K. Alshammari, Y. Niu, R. E. Palmer, N. Dimitratos, in *Philos. Trans. R. Soc. A Math. Phys. Eng. Sci.*, Royal Society Publishing, **2020**, p. 20200057.
- [14] Y. Xu, Y. Wang, Y. Ding, L. Luo, X. Liu, Y. Zhang, *J. Appl. Electrochem.* **2013**, *43*, 679–687.
- [15] P. Deng, Z. Xu, Y. Feng, J. Li, *Sens. Actuators B* **2012**, *168*, 381–389.
- [16] P. Murugaesan, P. Aravind, N. Guruswamy Muniyandi, S. Kandasamy, *Environ. Technol.* **2015**, *36*, 2618–2627.
- [17] S. M. Ansar, C. L. Kitchens, *ACS Catal.* **2016**, *6*, 5553–5560.
- [18] V. D. A. Pedrosa, L. Codognoto, L. A. Avaca, in *J. Braz. Chem. Soc.*, Sociedade Brasileira De Quimica, **2003**, pp. 530–535.
- [19] C. Kästner, A. F. Thünemann, *Langmuir* **2016**, *32*, 7383–7391.
- [20] R.-S. Kühnel, D. Reber, C. Battaglia, *J. Electrochem. Soc.* **2020**, *167*, 070544.
- [21] L. E. Oi, M. Y. Choo, H. V. Lee, H. C. Ong, S. B. A. Hamid, J. C. Juan, *RSC Adv.* **2016**, *6*, 108741–108754.
- [22] R. Su, L. Kesavan, M. M. Jensen, R. Tiruvalam, Q. He, N. Dimitratos, S. Wendt, M. Glasius, C. J. Kiely, G. J. Hutchings, F. Besenbacher, *Chem. Commun.* **2014**, *50*, 12612–12614.
- [23] R. Su, R. Tiruvalam, Q. He, N. Dimitratos, L. Kesavan, C. Hammond, J. A. Lopez-Sanchez, R. Bechstein, C. J. Kiely, G. J. Hutchings, F. Besenbacher, *ACS Nano* **2012**, *6*, 6284–6292.
- [24] F. Dionigi, P. Strasser, F. Dionigi, P. Strasser, *Adv. Energy Mater.* **2016**, *6*, 1600621.
- [25] R. Su, R. Tiruvalam, A. J. Logsdail, Q. He, C. A. Downing, M. T. Jensen, N. Dimitratos, L. Kesavan, P. P. Wells, R. Bechstein, H. H. Jensen, S. Wendt, C. R. A. Catlow, C. J. Kiely, G. J. Hutchings, F. Besenbacher, *ACS Nano* **2014**, *8*, 3490–3497.
- [26] L. Sobhana, M. Sarakha, V. Prevot, P. Fardim, *Appl. Clay Sci.* **2016**, *134*, 120–127.
- [27] L. S. Sobhanadhas, L. Kesavan, M. Lastusaari, P. Fardim, *ACS Omega* **2019**, *4*, 320–330.
- [28] L. S. Liji, R. Mehedi, M. Malmivirta, P. Paturi, M. Lastusaari, M. M. Dîrtu, Y. Garcia, P. Fardim, *Appl. Clay Sci.* **2016**, *132–133*, 641–649.
- [29] A. O. Koyejo, L. Kesavan, P. Damlin, M. Salomäki, J. G. Yao, M. Hakkarainen, C. Kvarnström, *ChemElectroChem* **2020**, *7*, 4889–4899.
- [30] L. Sobhana, L. Kesavan, J. Gustafsson, P. Fardim, *Beilstein J. Nanotechnol.* **2019**, *10*, 589.
- [31] T. Theivasanthi, M. Alagar, **2013**.
- [32] E. Filippo, C. Carlucci, A. L. Capodilupo, P. Perulli, F. Conciauro, G. A. Corrente, G. Gigli, G. Ciccarella, *Mater. Res.* **2015**, *18*, 473–481.
- [33] Y. Wang, L. Li, X. Huang, Q. Li, G. Li, *RSC Adv.* **2015**, *5*, 34302–34313.
- [34] L. Huang, C. Megias-Sayago, R. Bingre, Q. Zheng, Q. Wang, B. Louis, *ChemCatChem* **2019**, *11*, 3279–3286.
- [35] D. Dumbre, V. R. Choudhary, P. R. Selvakannan, *Polyhedron* **2016**, *120*, 180–184.
- [36] J. Yu, X. Zhao, J. C. Yu, G. Zhong, J. Han, Q. Zhao, *The Grain Size and Surface Hydroxyl Content of Super-Hydrophilic TiO<sub>2</sub>/SiO<sub>2</sub> Composite Nanometer Thin Films*, **2001**.
- [37] D. X. Martínez Vargas, J. Rivera De la Rosa, C. J. Lucio-Ortiz, A. Hernández-Ramírez, G. A. Flores-Escamilla, C. D. Garcia, *Appl. Catal. B* **2015**, *179*, 249–261.
- [38] M. Rahulan, S. Ganesan, P. Aruna, *Adv. Nat. Sci. Nanosci. Nanotechnol. Adv. Nat. Sci. Nanosci. Nanotechnol* **2011**, *2*, 25012–25018.
- [39] A. Jawad, Z. Liao, Z. Zhou, A. Khan, T. Wang, J. Ifthikar, A. Shahzad, Z. Chen, Z. Chen, *ACS Appl. Mater. Interfaces* **2017**, *9*, 28451–28463.
- [40] F. Su, T. Wang, R. Lv, J. Zhang, P. Zhang, J. Lu, J. Gong, *Nanoscale* **2013**, *5*, 9001–9009.
- [41] Y. Song, C. Wei, X. Zhang, X. Wei, X. Song, Z. Sun, *Mater. Chem. Phys.* **2015**, *161*, 153–161.
- [42] M. G. Rinaudo, A. M. Beltrán, M. A. Fernández, L. E. Cadús, M. R. Morales, *Chem. Proc.* **2020**, *2*, 13.
- [43] X. Geng, Y. Luo, B. Zheng, C. Zhang, *Int. J. Hydrogen Energy* **2017**, *42*, 6425–6434.
- [44] Y. Feng, Q. Shao, B. Huang, J. Zhang, X. Huang, *Natl. Sci. Rev.* **2018**, *5*, 895–906.
- [45] Q. Cheng, J. Xu, T. Wang, L. Fan, R. Ma, X. Yu, J. Zhu, Z. Xu, B. Lu, *Appl. Surf. Sci.* **2017**, *422*, 528–535.
- [46] S. Kang, R. Mauchauffé, Y. S. You, S. Y. Moon, *Sci. Rep.* **2018**, *8*, DOI 10.1038/S41598-018-35154-4.
- [47] Y. Gao, Z. Zhao, H. Jia, X. Yang, X. Lei, X. Kong, F. Zhang, *J. Mater. Sci. n.d.*, *54*, DOI 10.1007/s10853-019-03964-0.
- [48] L. Liu, S. Li, Y. An, X. Sun, H. Wu, J. Li, X. Chen, H. Li, *Catal.* **2019**, *9*, 118.
- [49] S. L. Candelaria, N. M. Bedford, T. J. Woehl, N. S. Rentz, A. R. Showalter, S. Pylpenko, B. A. Bunker, S. Lee, B. Reinhart, Y. Ren, S. P. Ertem, E. B. Coughlin, N. A. Sather, J. L. Horan, A. M. Herring, L. F. Greenlee, *ACS Catal.* **2017**, *7*, 365–379.
- [50] S. Dutta, A. Indra, Y. Feng, T. Song, U. Paik, *ACS Appl. Mater. Interfaces* **2017**, *9*, 33766–33774.
- [51] M. E. Tessensohn, H. Hirao, R. D. Webster, **2012**, DOI 10.1021/jp311007m.
- [52] P. A. Staley, C. M. Newell, D. P. Pullman, D. K. Smith, *Anal. Chem.* **2014**, *86*, 10917–10924.
- [53] D. S. Silvester, A. J. Wain, L. Aldous, C. Hardacre, R. G. Compton, *J. Electroanal. Chem.* **2006**, *596*, 131–140.
- [54] C. L. Forryan, R. G. Compton, **n.d.**, DOI 10.1039/b307553m.
- [55] C. Amatore, J. M. Savéant, G. Capobianco, G. Farnia, G. Sandonà, M. G. Severin, E. Vianello, *J. Am. Chem. Soc.* **1985**, *107*, 1815–1824.
- [56] G. Farnia, A. Roque Da Silva, E. Vianello, *J. Electroanal. Chem. Interfacial Electrochem.* **1974**, *57*, 191–202.
- [57] L. Kesavan, R. Tiruvalam, M. H. A. Rahim, M. I. Bin Saiman, D. I. Enache, R. L. Jenkins, N. Dimitratos, J. A. Lopez-Sanchez, S. H. Taylor, D. W. Knight, C. J. Kiely, G. J. Hutchings, *Science* **2011**, *331*, 195–199.
- [58] S. Ramaraj, S. Mani, S. M. Chen, S. Palanisamy, V. Velusamy, J. M. Hall, T. W. Chen, T. W. Tseng, *Sci. Rep.* **2018**, *8*, 2–10.
- [59] C. L. Forryan, N. S. Lawrence, N. V. Rees, R. G. Compton, *J. Electroanal. Chem.* **2004**, *561*, 53–65.
- [60] L. Dou, H. Zhang, *J. Mater. Chem. A* **2016**, *4*, 18990–19002.
- [61] H. Li, L. Han, J. Cooper-White, I. Kim, *Green Chem.* **2012**, *14*, 586–591.
- [62] A. F. Baye, D. H. Han, S. K. Kassahun, R. Appiah-Ntiamoah, H. Kim, *Electrochim. Acta* **2021**, *398*, 139343.

Manuscript received: April 22, 2022  
Revised manuscript received: May 18, 2022  
Accepted manuscript online: May 19, 2022